Acta Crystallographica Section D
Biological Crystallography
ISSN 0907-4449

Diffraction cartography: applying microbeams to macromolecular crystallography sample evaluation and data collection

Matthew W. Bowler,[a]* Matias Guijarro,[a] Sebastien Petitdemange,[b] Isabel Baker,[a,c] Olof Svensson,[a] Manfred Burghammer,[b] Christoph Mueller-Dieckmann,[a] Elspeth J. Gordon,[a] David Flot,[a] Sean M. McSweeney[a] and Gordon A. Leonard[a]

[a]Structural Biology Group, European Synchrotron Radiation Facility, 6 Rue Jules Horowitz, F-38043 Grenoble, France, [b]Structure of Soft Matter Group, European Synchrotron Radiation Facility, 6 Rue Jules Horowitz, F-38043 Grenoble, France, and [c]Department of Biology and Biochemistry, University of Bath, Claverton Down, Bath BA2 7AY, England

Correspondence e-mail: bowler@esrf.fr

Received 9 March 2010
Accepted 25 May 2010

Crystals of biological macromolecules often exhibit considerable inter-crystal and intra-crystal variation in diffraction quality. This requires the evaluation of many samples prior to data collection, a practice that is already widespread in macromolecular crystallography. As structural biologists move towards tackling ever more ambitious projects, new automated methods of sample evaluation will become crucial to the success of many projects, as will the availability of synchrotron-based facilities optimized for high-throughput evaluation of the diffraction characteristics of samples. Here, two examples of the types of advanced sample evaluation that will be required are presented: searching within a sample-containing loop for microcrystals using an X-ray beam of 5 µm diameter and selecting the most ordered regions of relatively large crystals using X-ray beams of 5–50 µm in diameter. A graphical user interface developed to assist with these screening methods is also presented. For the case in which the diffraction quality of a relatively large crystal is probed using a microbeam, the usefulness and implications of mapping diffraction-quality heterogeneity (diffraction cartography) are discussed. The implementation of these techniques in the context of planned upgrades to the ESRF's structural biology beamlines is also presented.

1. Introduction

It is very common for crystals of biological macromolecules, even when obtained under apparently identical conditions, to show variation in the quality of their diffraction. This variation is almost certainly the result of the intrinsic physical properties of the systems being studied. The molecules involved are often flexible, leading to conformational heterogeneity. In the case of complexes of several proteins there is also the possibility of compositional heterogeneity, in which some complexes within the crystal have lost components (see, for example, Cramer *et al.*, 2000; Wimberly *et al.*, 2000). Moreover, as crystals of biological macromolecules are often mechanically fragile and therefore susceptible to damage during transfer (from crystallization trays to sample holders) or essential cryoprotection steps, diffraction quality can vary within a crystal. This is especially evident when diffraction is probed with a micrometre X-ray beam (Cusack *et al.*, 1998; Higuchi *et al.*, 1996; Sanishvili *et al.*, 2008). It is therefore not uncommon that a large number of samples, often thousands, have to be

evaluated to find the crystals, or regions of crystals, with the diffraction properties required to answer the biological question being asked. To increase the chances of a successful outcome of a diffraction data-collection experiment, particularly in the study of more problematic systems, sample evaluation (Leslie *et al.*, 2002) has become widespread and automated in macromolecular crystallography (MX; Arzt *et al.*, 2005; Zhang *et al.*, 2006; Okazaki *et al.*, 2008; Snell *et al.*, 2004; Soltis *et al.*, 2008; McPhillips *et al.*, 2002). Indeed, the automation of beam delivery (Nurizzo *et al.*, 2006; Gabadinho *et al.*, 2010; McPhillips *et al.*, 2002), sample mounting (Cipriani *et al.*, 2006; Ohana *et al.*, 2004; Snell *et al.*, 2004), crystal centring in the X-ray beam (Lavault *et al.*, 2006; Pothineni *et al.*, 2006) and sample evaluation and ranking (Incardona *et al.*, 2009; Leslie *et al.*, 2002; Popov & Bourenkov, 2003) has allowed the evaluation of numbers of samples that were unimaginable only five years ago and has led to a fundamental change in the way that structural biology beamlines are used. At the ESRF, a dramatic increase in the number of samples that are tested for diffraction quality before any complete data collections are carried out has been observed (Fig. 1). Moreover, the success of many high-profile projects has been dependent on the evaluation of many thousands of samples before data sets are collected (Selmer *et al.*, 2006; Warne *et al.*, 2008; Ben-Shem *et al.*, 2003; Sibanda *et al.*, 2010) and access to highly automated high-throughput evaluation facilities, with the additional possibility of then transferring the best crystals to another beamline optimized for data collection, will become an increasingly important element for success in structural biology. This implies the need for increasingly sophisticated hardware and software to evaluate, track, sort and redistribute samples and will rely heavily on developments to be made to databases such as ISPyB (Beteva *et al.*, 2006), sample-handling robots and evaluation software such as *EDNA* (Incardona *et al.*, 2009).

As sample evaluation, automation and microbeams have become more widely available, more advanced screening methods have evolved. These include locating the best region of a crystal on which to perform data collection (Higuchi *et al.*, 1996; Sanishvili *et al.*, 2008), locating and evaluating the diffraction properties of crystals in crystallization drops (Jacquamet *et al.*, 2004, 2009) and locating and evaluating the diffraction properties of very small crystals contained in large sample mounts (Cherezov *et al.*, 2009). These types of sample evaluation are already performed empirically by many crystallographers. However, at the ESRF we seek to formalize and automate these procedures, as we have done for other processes in MX experiments, and thus allow them to become routine. To achieve this goal requires the combination of current 'line' and 'mesh' scans (see Song *et al.*, 2007) with diffraction-quality characterization and experiment planning (Incardona *et al.*, 2009; Leslie *et al.*, 2002; Popov & Bourenkov, 2003) and 'playback' centring. Significant modifications to current sample-evaluation pipelines and to information-

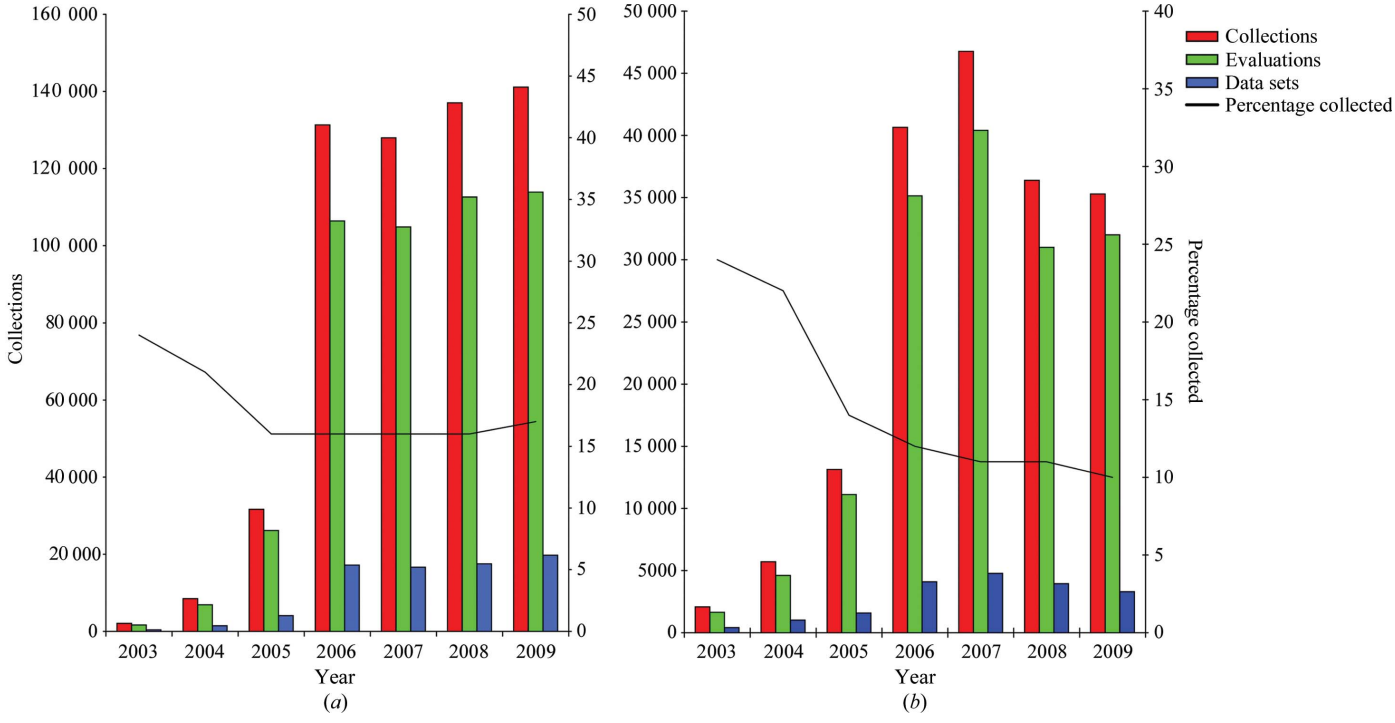

Figure 1
MX sample evaluation and data collection at the ESRF (data harvested from the ISPyB database). (*a*) The total numbers of collections, screenings and data sets are shown in the bar chart. The percentage of samples from which data were eventually collected is shown as a black line. An increase in the number of evaluations and a decrease in the percentage of samples from which data were collected is observed upon the introduction of the SC3 and *MXCuBE* (2005). (*b*) Beamlines ID14-1, ID14-2 and ID14-3 (ID14-3 was recommissioned as a bio-SAXS beamline at the end of 2007; therefore, statistics for 2008 and 2009 are for ID14-1 and ID14-2 only). These beamlines are heavily used for sample evaluation. The percentage of samples from which full data sets are collected has fallen steadily to 10% in 2009 (screens are defined as $\leq$4 images and a data set is defined as $\geq$30 images).

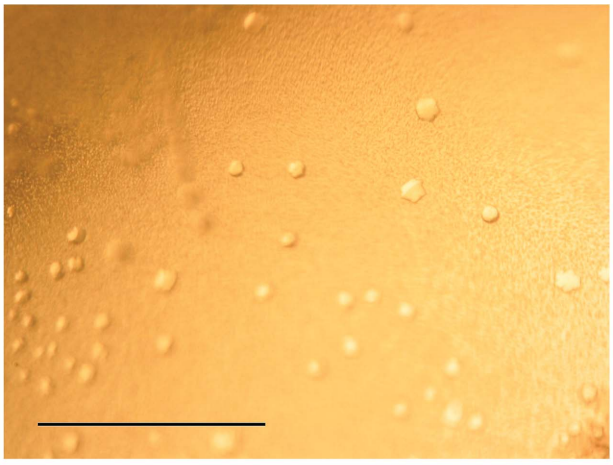

(*a*)

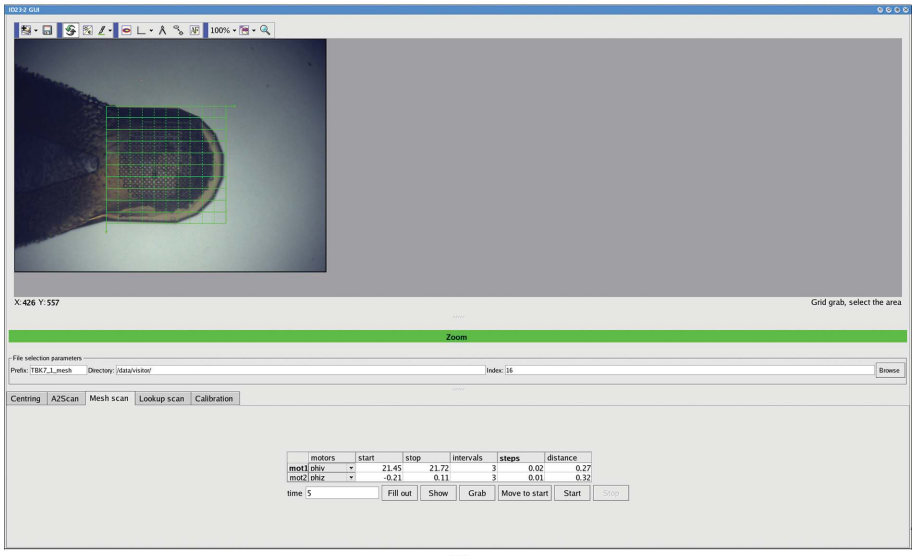

(*b*)

Figure 2
(*a*) Crystals of *E. coli* ATP synthase. The crystals are approximately 10 µm in the largest dimension. The scale bar represents 100 µm. (*b*) The ID23-2 GUI in the 'Mesh scan' tab. The GUI offers several options, usually only required when using a 5 µm beam, in combination with the on-axis view of the sample. The 'Centring' tab offers a centring guide line and 'n-click' centring; this option allows any number of positions to be used to increase the accuracy of centring. The 'A2scan option' will locate a crystal in a loop by diffraction or perform a line scan. The 'Mesh scan' option covers a defined area in a defined number of steps and the 'Lookup scan' option allows more complicated mesh-scan areas to be drawn.

management systems such as ISPyB (Beteva *et al.*, 2006) will also be required. Such modifications will form a central part of the developments to be made during the forthcoming upgrade of the ESRF's MX facilities (http://go.esrf.eu/Upgrade), in particular the provision of a set of beamlines optimized for high-throughput automated sample evaluation: the Massively Automated Sample Selection Integrated Facility (MASSIF).

Here, we describe significant advances in the automation of two of the techniques referred to above: locating and identifying microcrystals within a large loop and locating the best part of a large crystal on which to collect diffraction data. Building on the developments made at the ESRF microfocus beamline ID13 (Cusack *et al.*, 1998; Moukhametzianov *et al.*, 2008; Riekel *et al.*, 2005), software developed to assist in these types of screening is presented.

2. Experimental procedures and results

2.1. Lilliput: finding and identifying microcrystals in an opaque glass

For many projects, particularly those initially producing microcrystals, rapid identification of crystallization conditions that yield protein crystals is a considerable advantage. However, locating microcrystals within a much larger loop is problematic. Here, we describe the use of a mesh scan to locate and evaluate microcystals of *E. coli* ATP synthase.

2.1.1. Crystallization and preparation. The *unc*$^{-}$ strain of *Escherichia coli* DK8, bearing the plasmid pFV2 containing a cysteine-less ATP synthase, was kindly provided by Professor Stephen Vik (Department of Biological Sciences, Southern Methodist University, Dallas, USA). ATP synthase was expressed and purified by nickel-affinity chromatography as described previously (Ishmukhametov *et al.*, 2005). The protein was concentrated to 10 mg ml^{-1} and set up in sitting-drop crystallization trays. Crystals (10 µm in the largest dimension) appeared after one week (Fig. 2*a*); full experimental details will be described elsewhere. As the crystals were too small to allow normal handling, they were therefore cryocooled directly from the mother liquor and were not explicitly cryoprotected. To harvest crystals, the crystallization drops were swept with micromeshes (MiTeGen, Ithica, New York, USA), which were then plunged into liquid nitrogen and stored at 100 K. This procedure produced an opaque glass containing several microcrystals (Figs. 2*b* and 3*a*).

2.1.2. Location and evaluation of crystals. Viewing and centring microcrystals is challenging. Spherical aberration by the lens of the on-axis viewer makes it difficult to locate thin crystals with visible light and the lack of explicit cryoprotection (see above) often means that the resulting glass in which the microcrystals are contained is opaque. In such cases, the most convenient way to identify both the position and the composition (*i.e.* protein/not protein) of crystals is to use X-ray diffraction. In order to test whether the crystals obtained following the protocol outlined in §2.1.1 were of

protein or not, still diffraction images were collected at each point on a user-defined grid, taking advantage of the mesh-scan capability (*dmesh*) available in the low-level beamline-control software *SPEC* (Certified Scientific Software; http://www.certif.com). The scan was carried out on ESRF beamline ID23-2 (Flot *et al.*, 2010) using an X-ray beam of dimensions 7 × 5 µm. A graphical user interface (GUI) has been implemented to make this process user-friendly (Fig. 2*b*). In the sample-display area of the GUI, the limits of the grid are drawn using the mouse and a step size for sampling the grid is chosen. In the software each position in the grid is associated with a specific coordinate [expressed as the position of the motors *phiz* (vertical translation of the goniometer axis) and *phiy* (horizontal translation)] so that once a crystal has been located the position can easily be returned to. As a large number of crystals were present in the loop and to limit data-collection time, a rough scan using a step size of 40 µm was chosen for this experiment. After the scan was completed, approximately 100 images for each loop had been collected. Diffraction spots indicating that the samples were protein and that at least one crystallization condition was worth pursuing were observed in four of the images taken from one loop (Fig. 3).

2.2. Brobdingnag: diffraction cartography of large crystals

At modern synchrotron sources crystallographers are often provided with a beam that is smaller than the largest dimension of the crystal. This presents the problem of finding the best position within the crystal to centre to the X-ray beam. Here, we describe the use of a mesh scan combined with online data analysis and the intuitive presentation of the data to systematically define the most ordered part of a crystal.

2.2.1. Test-crystal preparation. Crystals of bovine mitochondrial F_1-ATPase, grown as described previously (Lutter *et al.*, 1993) with the exception that azide was omitted from all buffers, were kindly provided by Mr Martin Montgomery and Professor Sir John Walker (MRC Mitochondrial Biology Unit, Cambridge, England). Several of these crystals with approximate dimensions of 500 × 400 × 50 µm were mounted on micromesh loops (MiTeGen, Ithica, New York, USA) and conditioned with the HC1b humidity-control device (Sanchez-Weatherby *et al.*, 2009) mounted on ESRF beamline ID14-2, using conditions previously established for maximum improvement in crystal diffraction properties (Bowler *et al.*, 2006*b*). Crystals were cryocooled directly after conditioning without any cryoprotectant.

Crystals of thermolysin were grown according to established protocols (Mueller-Dieckmann *et al.*, 2005). Briefly, *B. thermoproteolyticus* thermolysin (Sigma, St Louis, USA) was dissolved in 50 m*M* MES pH 6.0 and 45% DMSO and adjusted to a concentration of 50 mg ml^{-1}. This solution was then mixed in a 1:1 ratio with a solution consisting of 50 m*M* MES pH 6.0, 1 *M* NaCl and 45% DMSO and equilibrated against a reservoir buffer consisting of 35% saturated ammonium sulfate in hanging drops. Large crystals appeared after a few days and were cryoprotected in paraffin oil.

Crystals of β_1-andregenic G-protein-coupled receptor from turkey, prepared as described by Warne *et al.* (2008), were kindly provided by Dr Tony Warne and Dr Chris Tate (MRC Laboratory of Molecular Biology, Cambridge, England).

2.2.2. Intra-crystal diffraction heterogeneity of a crystal of bovine mitochondrial F_1-ATPase. Crystals of bovine mitochondrial F_1-ATPase tend to diffract rather weakly ($d_{\rm min} \simeq 3$ Å) and demonstrate considerable variation in the quality of their diffraction. Conditioning these crystals by controlled dehydration reduces the unit-cell volume by 20% and signif-

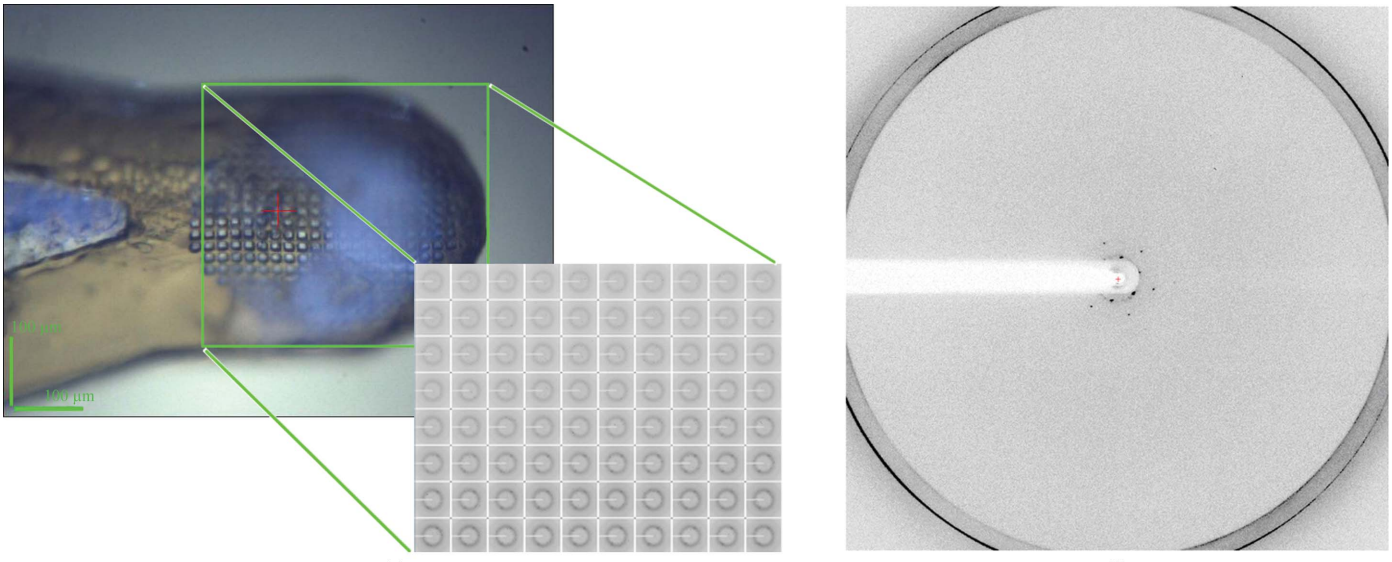

(*a*) (*b*)

Figure 3
Locating and evaluating 10 µm crystals in an opaque solution. (*a*) A grid screen was implemented in the ID23-2 GUI and diffraction images were obtained for each position. (*b*) One of four images that demonstrated weak diffraction, defining the location of crystals and indicating that the samples contained protein.

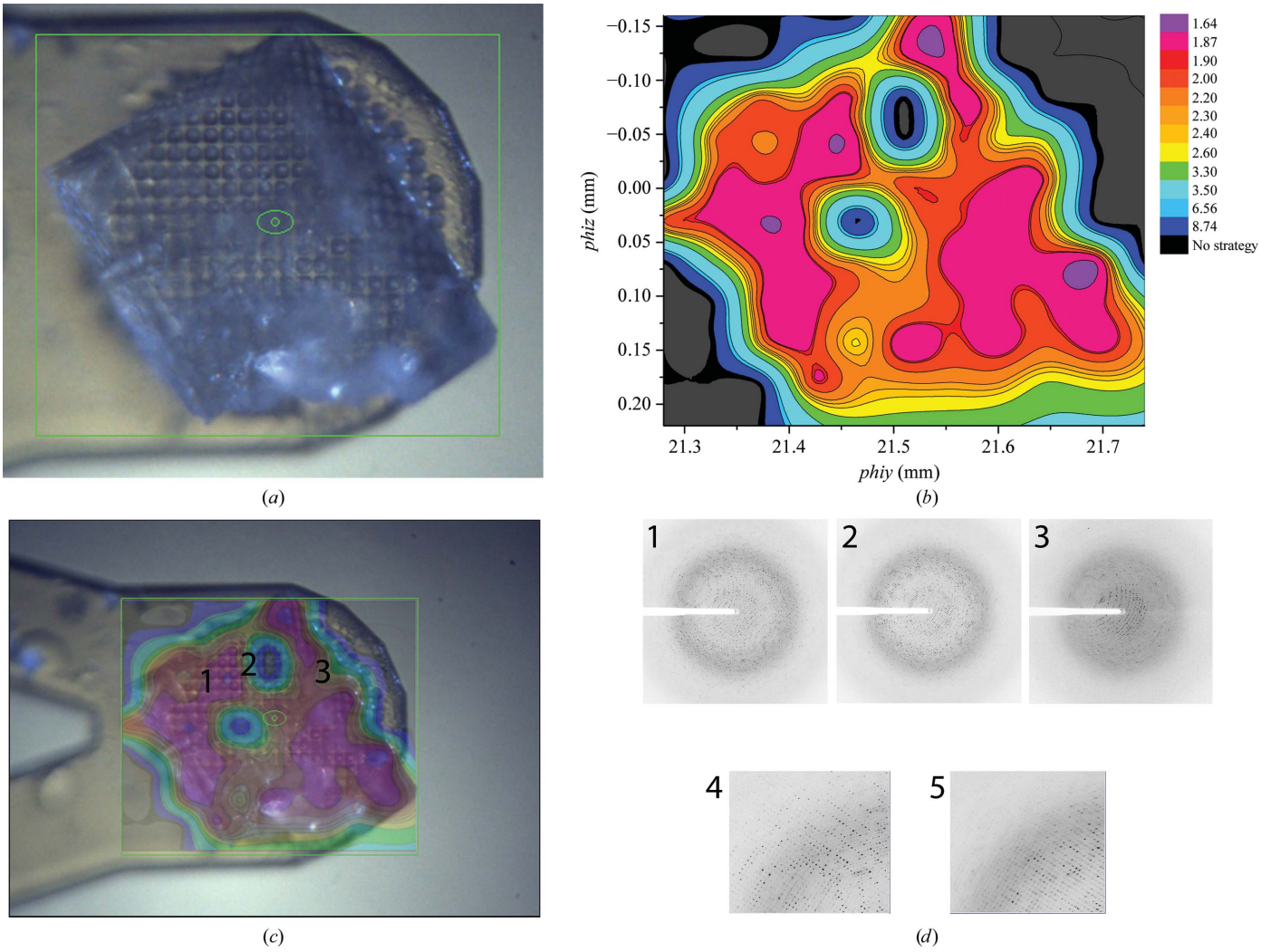

Figure 4
Diffraction cartography of a single crystal of bovine mitochondrial F_1-ATPase. (*a*) A grid scan was implemented over the area of the crystal (green box) with 40 µm steps (the beam size and position is shown by a green ellipse). (*b*) Images were processed with *EDNA* and the ranking resolution (coloured blue to mauve) was plotted against the motor positions *phiy* and *phiz*. Contour lines mark areas of equal diffraction quality. The maximum total exposure time allowed for a data collection was arbitrarily chosen to be 1200 s. (*c*) Overlay of the diffraction map on the crystal image; the shape of the crystal is well defined by the grid scan. Numbers are placed to the left of the positions from which diffraction images are shown in (*d*). Example diffraction images from the scan; the numbers correspond to the positions indicated in (*c*). 4 and 5 show the same magnified area of the detector from images 1 and 2, highlighting the difference in diffraction quality.

icantly increases both the diffraction limit ($d_{\rm min} \simeq 1.8$ Å) and the quality of the Bragg peaks (Bowler *et al.*, 2006*a*, 2007; Sanchez-Weatherby *et al.*, 2009). Despite these improvements in diffraction quality, the crystals remain rather sensitive to radiation damage and the collection of a full data set to the highest possible resolution is often not possible from a single position within a crystal. Moreover, intra-crystal variability in diffraction quality (Higuchi *et al.*, 1996; Sanishvili *et al.*, 2008) means that it is not always evident at which positions within a crystal the highest resolution or best-quality diffraction data can be collected. We therefore used a modified mesh-scan procedure to map the diffraction-quality heterogeneity of crystals of bovine mitochondrial F_1-ATPase, again using an X-ray beam of dimensions 7 × 5 µm on ID23-2. The protocol used 40 µm steps and at each grid point an automatic script was used to carry out an *EDNA*/*BEST* (Incardona *et al.*, 2009; Leslie *et al.*, 2002; Popov & Bourenkov, 2003) characterization of diffraction quality. The 'ranking resolution[1]' was then plotted against grid position[2]. The results from this procedure, which are shown as a contour map in Fig. 4, are extremely instructive. Diffraction quality, as probed with a microbeam, varies markedly across the crystal surface and is particularly poor in some regions. While the map is necessarily an interpolation of the results at each grid point, the diffraction map obtained clearly suggests regions of the crystal which should be exposed to X-rays in order to collect the best diffraction

[1] Ranking resolution is defined as the predicted maximum resolution available [$\langle I/\sigma(I)\rangle \geq 3$ in the highest resolution bin] in the total exposure time allowed for a data collection.
[2] A series of diffraction images linked with the grid scan, crystal image and beam position presented as a movie has been deposited as supplementary material.

data. It is interesting to note that the areas exhibiting the highest ranking resolution also tend to share similar unit-cell parameters (Fig. S1[3]). The *b* and *c* unit-cell parameters vary considerably across the crystal (probably owing to incomplete phase transitions induced by dehydration) but are very similar in highly ordered areas, regardless of their physical location. While this does not necessarily indicate isomorphism between different regions of the crystal, it does suggest that data could be merged from the multiple sites of similar diffraction quality to obtain a complete data set.

When developing the protocol described above, considerable thought was given as to the best criterion to use as an indicator of diffraction quality. In the diffraction-based centring protocol developed by Song *et al.* (2007), the number of 'good' diffraction spots observed inside a limited resolution range was used. In our experience, however, such a criterion does not exclude positions in a crystal which exhibit multiple lattices. We have thus chosen to execute a full *EDNA*/*BEST* characterization of the diffraction quality at each grid point in the scan and to use the 'ranking resolution' as the criterion for ranking diffraction quality. While this approach is slower (∼5 s per image for a full characterization) than spot-finding-based algorithms, such a strategy has a number of advantages: regions in a crystal which exhibit multiple lattices result in a failure at the autoindexing stage (as a result of too high an r.m.s. deviation between calculated and observed spot positions); the resulting 'diffraction-quality' map allows the ranking of different regions of the crystal and makes multi-position data-collection strategies feasible; the maps also highlight larger areas of similar diffraction quality which could be used to determine a region of a crystal in which 'helical' data-collection protocols (Flot *et al.*, 2010) could be most usefully employed.

The diffraction-quality map shown in Fig. 4 was obtained in only one orientation: with the smallest dimension of the crystal perpendicular to the X-ray beam. While such a map would be useful for planning data-collection strategies for crystals with high-symmetry space groups, it is clear that for crystals of lower symmetry the computation of diffraction-quality maps in two mutually perpendicular orientations is required. We therefore carried out mesh scans on a smaller crystal of bovine F_1-ATPase (∼200 µm in the largest dimension) in two dimensions (Fig. 5). These scans used a 50 µm aperture on beamline ID29 with a 50 µm step size and were therefore of a much lower spatial resolution than those obtained using a smaller beam. The characterization of images also included an exposure time limited by the maximum X-ray dose calculated by *RADDOSE* (Paithankar *et al.*, 2009). Scanning a second dimension shows that the best position in one dimension does not necessarily overlap with that in the second.

A successful strategy is therefore to first centre on the best area of the crystal determined from diffraction where the largest dimension is positioned parallel to the X-ray beam and then centre on the best position in the second dimension found on the line of *phiy* (horizontal translation) determined from diffraction through the largest dimension. In this manner, and based on a subsequent data-collection strategy calculated using *EDNA*/*BEST*, we were able to collect a complete data set to $d_{\min} = 2.09$ Å in a single contiguous sweep (Table 1). It is rather unlikely that the region of the crystal used for data collection would have been chosen without the aid of the calculated diffraction-quality maps. Combining orthogonal mesh scans also allows recovery of the three-dimensional shape and diffraction properties of the crystal (Fig. 5*c*; §3).

Table 1
Data-collection statistics for the F_1-ATPase crystal shown in Fig. 5.

Values in parentheses are for the highest resolution bin.

Space group	$P2_12_12_1$
Wavelength (Å)	0.976
Unit-cell parameters (Å)	$a = 105.8$, $b = 126.9$, $c = 261.6$
Resolution range (Å)	20–2.09 (2.21–2.09)
No. of unique reflections	192537
Multiplicity	3.9 (3.7)
Completeness	93.3 (83.5)
$R_{\rm merge}$†	0.11 (0.77)
$\langle I/\sigma(I)\rangle$	8.1 (1.7)

† $R_{\rm merge} = \sum_{hkl}\sum_i |I_i(hkl) - \langle I(hkl)\rangle| / \sum_{hkl}\sum_i I_i(hkl)$, where $\langle I(hkl)\rangle$ is the mean weighted intensity after rejection of outliers.

2.2.3. Intra-crystal diffraction heterogeneity of a crystal of thermolysin. To test the general effectiveness of the generation of diffraction heterogeneity maps, we carried out our analysis on some other systems. The first of these was a long needle-shaped crystal (dimensions ∼500 × 50 × 50 µm) of thermolysin prepared and cryocooled as described in §2.2.1. Here, diffraction properties were probed using an X-ray beam 30 × 30 µm in size and a mesh-scan step size of 30 µm on ID29. In a slight modification to the scanning protocol, a 1° oscillation image was taken at each grid point. An automatic script was again used to carry out an *EDNA*/*BEST* characterization of diffraction quality and the 'ranking resolution' was plotted against grid position. The diffraction map showing the disposition of the crystal and the resulting ranking resolution map are shown in Fig. 6. As can be seen, crystal diffraction quality varies through the needle axis of the crystal. The ranking resolution limits are ∼1.5 Å towards both ends of the crystal and ∼1.7 Å towards the middle. Although the variations seen are not as large as those for the crystal of F_1-ATPase, they are nevertheless significant and may be particularly important in the study of protein–ligand interactions, where it is normally desirable to obtain the highest resolution data possible.

2.2.4. Intra-crystal diffraction heterogeneity of a crystal of β_1-andregenic G-protein-coupled receptor. The validity of the technique has been demonstrated for two well diffracting cases; however, is the method viable with the most challenging proteins? To investigate the robustness of diffraction cartography, the technique was performed on crystals of the β_1-andregenic G-protein-coupled receptor. Membrane-

[3] Supplementary material has been deposited in the IUCr electronic archive (Reference: EA5122). Services for accessing this material are described at the back of the journal.

protein crystals usually have very weak interactions between molecules and, coupled with the dynamic nature of G-protein-coupled receptors, this leads to considerable variation between and within crystals that diffract very poorly (Gether *et al.*, 1997; Warne *et al.*, 2008). The crystals are thin plates with approximate dimensions of 200 × 100 × 10 µm. A scan was launched on a single crystal of β_1-andregenic G-protein-coupled receptor (Fig. 7*a*) using an X-ray beam 15 × 15 µm in size and a mesh-scan step size of 15 µm on ID29. The diffraction patterns were analysed using *EDNA*/*BEST*; however, the diffraction in most areas was very poor and to low resolution. As *BEST* is unable to determine the *B* factor from test images showing diffraction below 6 Å resolution, this led to a failure to calculate a ranking resolution in most areas. Therefore, the mosaic spread was used to map crystal order and shape (Figs. 7*b* and 7*c*). Again, the diffraction map defines the shape of the crystal and considerable variation in the quality of the diffraction was observed, with large areas in which indexing was not possible. Nevertheless, strategies could be calculated for four positions within the crystal with ranking resolutions of 2.78, 6.26, 3.47 and 6.63 Å, clearly identifying the best area for data collection.

3. Discussion

Above, we present two means of exploiting the micro and mini X-ray beams now routinely available to structural biologists at synchrotron sources when combined with mesh-scanning procedures. The first of these is the automatic location of microcrystals in large loops. An increasingly important requirement in MX is the identification of initial crystallization hits. This identification procedure falls into two

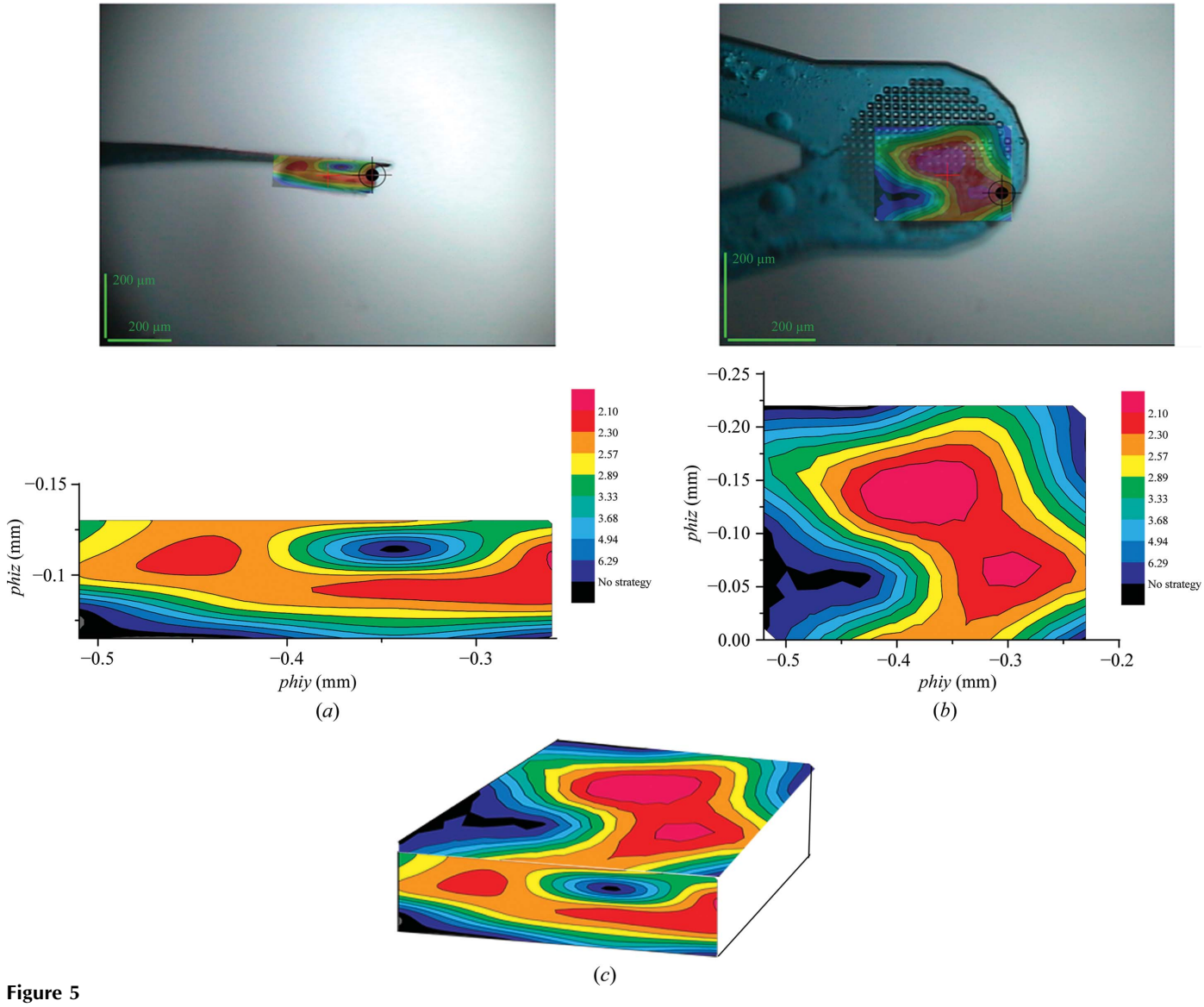

Figure 5
Diffraction-quality maps calculated in two orthogonal orientations for a crystal of F_1-ATPase. (*a*, *b*) The maps are superimposed on the crystal as seen from the point of view of the X-ray beam. Larger representations of the two maps obtained are also shown. For data collection the crystal was centred at the two positions marked. *EDNA*/*BEST* characterization at each grid point was carried out with a total exposure time calculated using the program *RADDOSE*. (*c*) Combining the orthogonal maps allows recovery of the three-dimensional shape and diffraction properties of the crystal.

categories: whether the objects are protein and which of the conditions provides the best diffracting sample. The pre-screening of microcrystals obtained from robotic crystallization trials, either in loops or the crystallization drop itself, will become more important in the future in order to feed information back into crystallization experiments. The combination of micrometre-sized beams and high levels of automation will be essential to such crystal-identification protocols.

The second technique we outline is the mapping of the intra-crystal diffraction heterogeneity of large (relative to the beam size) crystals; we call this diffraction cartography. Microbeams are increasingly being exploited for larger crystals to try to alleviate the fundamental problem of radiation damage in MX as they allow the possibility of collecting complete data sets by exposing multiple parts of the same crystal or multiple crystals within the same loop. In cases where diffraction quality varies significantly within the crystal

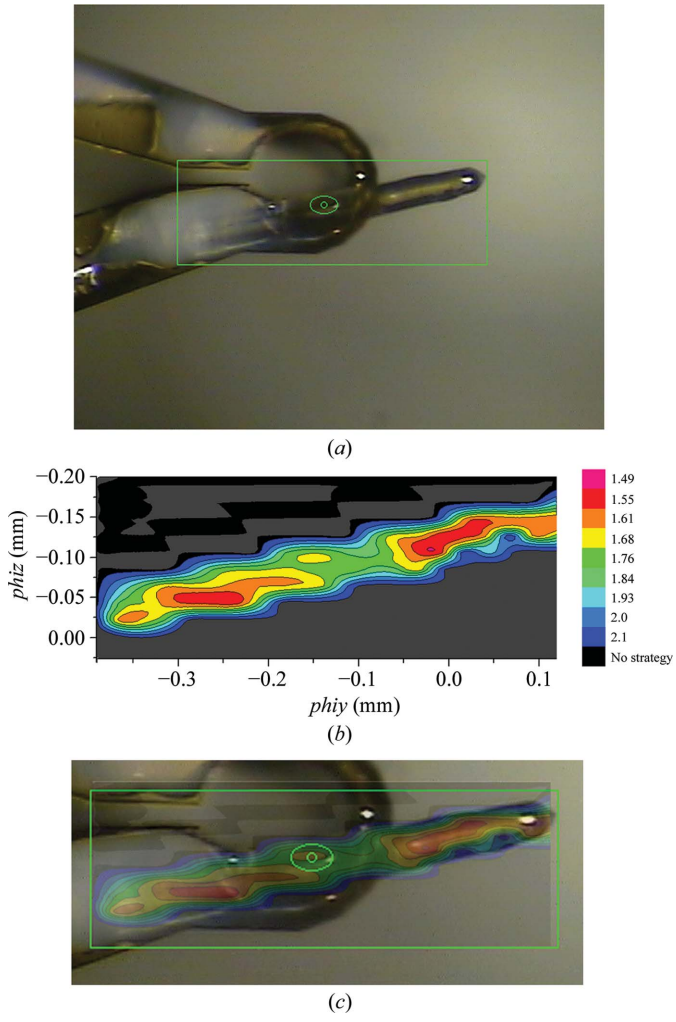

Figure 6
Diffraction cartography of a crystal of thermolysin. A grid scan was implemented over the area of the crystal (green box) (*a*) with 30 µm steps and a contour map was calculated as before (*b*). While the variation in diffraction is not as large as observed in F_1-ATPase, there is nevertheless significant variation, particularly in the area in contact with the mount. The map also defines the location and shape of the crystal (*c*).

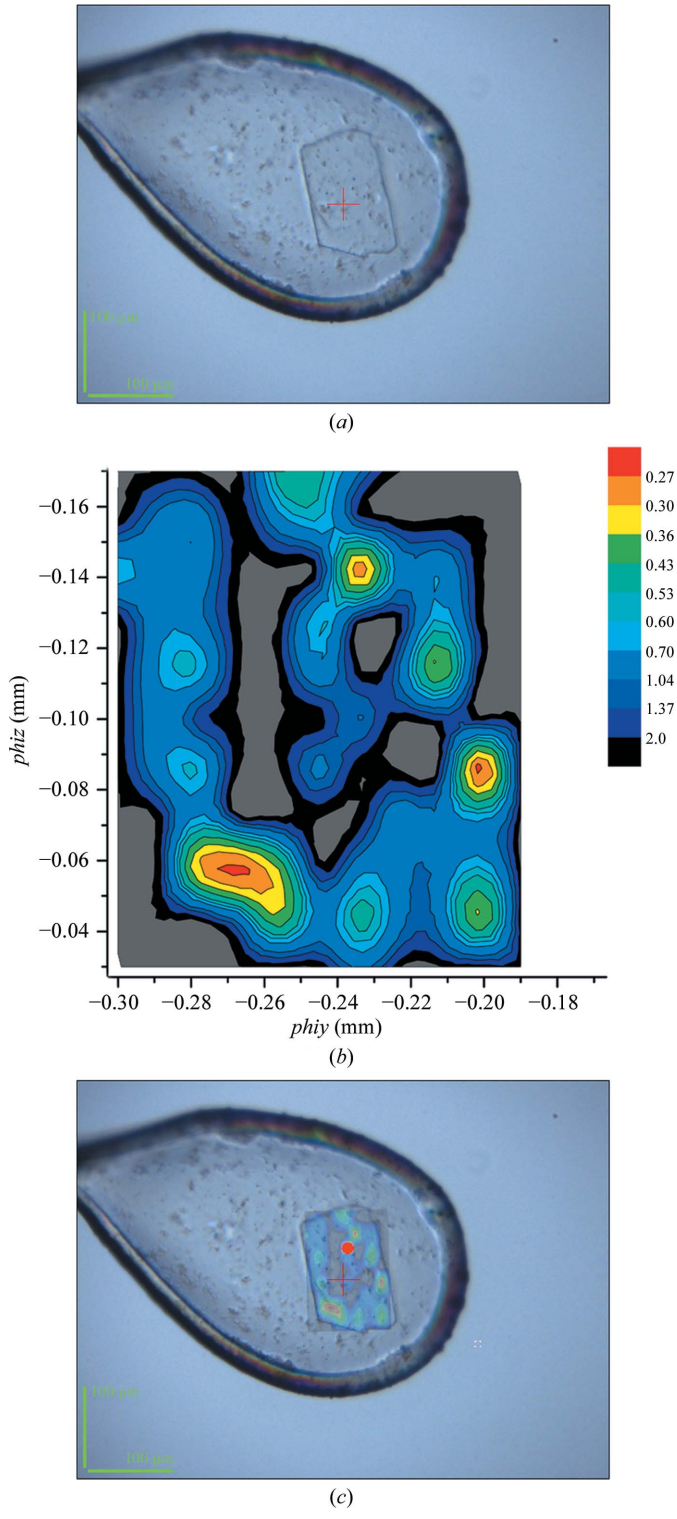

Figure 7
Diffraction cartography of a crystal of β1-andregenic G-protein-coupled receptor. A grid scan was implemented over the area of the crystal (*a*) with 15 µm steps and a diffraction map (*b*) was calculated as before but using the mosaic spread values (black to red) rather than the ranking resolution. There is significant variation in the quality of the crystal, with large areas in the middle in which indexing failed. The map again defines the location and shape of the crystal (*c*); a 15 µm red spot marks the position with a ranking resolution of 2.78 Å.

they are also being used to pick out the 'best' part of a larger crystal in order to improve the quality of the diffraction data obtainable. However, while the evaluation of sample diffraction quality using software packages such as *DNA*/*EDNA* is now routine, the use of such tools tends to be carried out on (at most) a relatively small number of positions on any given crystal and current methods of diffraction-quality screening are not suited to a systematic analysis of the diffraction landscape of a crystal or of a loop containing several microcrystals. Combining the use of microbeams with mesh scans and diffraction-quality characterization software such as *DNA* and *EDNA* allows diffraction landscapes to be calculated. Analysis of these landscapes makes the choice of regions in a large crystal from which to collect data no longer a matter of chance as diffraction quality at hundreds of positions within a crystal can be evaluated. The routine calculation of diffraction landscapes should result in a more efficient use of synchrotron beam time because complete data sets can be collated by collecting from as few regions as possible to the highest possible resolution from any given crystal. Faced with a crystal larger than the X-ray beam, most crystallographers would centre the middle of the crystal in the beam or at another position that seems to be morphologically best suited. The results from the examples presented here show that in many cases this may not produce the best possible data set from the sample.

The fast visualization of the diffraction-quality map of a crystal increases the possibilities available concerning data collection: a single grid point can be quickly selected for a single-sweep data collection, a larger area of similar diffraction quality can be used in conjunction with 'helical' data-collection protocols (Flot *et al.*, 2010) to produce a data set with minimized radiation damage and a full data set can be collated from partial data sets collected at various previously identified positions within a crystal. Work is under way to incorporate both the ID23-2 GUI and software enabling the online analysis of images and display of diffraction-quality maps into *MxCuBE* (Gabadinho *et al.*, 2010). The results of the intra-crystal characterization, mesh-scan motor positions and diffraction maps will be stored in ISPyB.

Diffraction cartography not only provides a useful map of crystal quality but also (as is the case for diffraction-based crystal-centring protocols; Song *et al.*, 2007) defines the shape of the crystal (Figs. 4, 5, 6 and 7). This can be useful in the implementation of absorption-correction protocols. While X-ray tomography (Brockhauser *et al.*, 2008) and reconstruction of optical images (Leal *et al.*, 2008) have also been used to define crystal shape, these methods require time-consuming rearrangements of the beamline, special detectors and/or specialized reconstruction programs and do not provide information regarding the diffraction characteristics of all or a region of a crystal. Diffraction cartography provides information on both the internal order and the physical shape of a crystal in a single experiment using the hardware generally available on a modern MX beamline. Clearly, the resolution of the crystal shape recovered depends on both the beam and the mesh-scan step size. Experiments are under way to determine the usefulness of crystal-shape determination using mesh scans in absorption-correction protocols.

Both of the methods we describe above represent new advanced methods of sample evaluation. These methods, and the sophisticated multisweep multicrystal data-collection strategies that will in many cases result from these protocols, will place much greater emphasis on the use of experimental metadata. The challenges presented by advanced sample evaluation to synchrotron hardware and software will be tackled by the MASSIF project. These beamlines, proposed as part of the ESRF Upgrade, will provide a set of highly automated beamlines optimized for high-throughput sample evaluation and the types of advanced screening described above. Three stations will directly address the fundamental problem of inter-sample and intra-sample variability in structural biology and will have different beam sizes: two stations with a 100 µm beam diameter and one microbeam station with a beam size 10–20 µm in diameter. Sample handling and transfer will be based on a moving-arm robot (Ohana *et al.*, 2004) in order to increase the capacity, throughput and types of compatible crystal mount (*e.g.* crystallization trays) of the beamlines. The 'outsourcing' of sample evaluation to these specialized beamlines will free time, of both scientists and beamlines, to be spent on collecting better quality data on beamlines optimized for specific requirements such as low signal-to-noise anomalous scattering experiments, large unit cells or microbeam MAD experiments.

After visiting Lilliput and Brobdingnag, Gulliver is rescued by the Kingdom of Laputa, a land dedicated to the study of science and the arts but completely unable to make practical use of their developments. Here, we hope that the integration of advanced screening techniques into the automated environment developed for MX experiments at the ESRF will allow highly challenging experiments to become practical by making these experiments routine rather than unusual.

The mesh scans and GUI described here were initially developed as part of a Long Term Project at the ESRF beamline ID13 awarded to Dr Christien Riekel (ESRF, Grenoble, France) and Professor Gebhard Schertler (MRC-LMB, Cambridge, UK) partly funded by a Human Frontiers Science Program Award. We thank Professor Sir John Walker and Mr Martin Montgomery (MRC Mitochondrial Biology Unit, Cambridge, England) and Dr Tony Warne and Dr Chris Tate (MRC Laboratory of Molecular Biology, Cambridge, England) for the very generous supply of crystals. We also thank Professor Stephen Vik (Southern Methodist University, Dallas, USA) for the *unc*$^{-}$ strain of *E. coli* DK8 bearing the plasmid pFV2 containing a cysteine-less ATP synthase.

References

Arzt, S. *et al.* (2005). *Prog. Biophys. Mol. Biol.* **89**, 124–152.
Ben-Shem, A., Frolow, F. & Nelson, N. (2003). *Nature (London)*, **426**, 630–635.
Beteva, A. *et al.* (2006). *Acta Cryst.* D**62**, 1162–1169.
Bowler, M. W., Montgomery, M. G., Leslie, A. G. W. & Walker, J. E. (2006*a*). *Proc. Natl Acad. Sci. USA*, **103**, 8646–8649.

Bowler, M. W., Montgomery, M. G., Leslie, A. G. W. & Walker, J. E. (2006*b*). *Acta Cryst.* D**62**, 991–995.
Bowler, M. W., Montgomery, M. G., Leslie, A. G. W. & Walker, J. E. (2007). *J. Biol. Chem.* **282**, 14238–14242.
Brockhauser, S., Di Michiel, M., McGeehan, J. E., McCarthy, A. A. & Ravelli, R. B. G. (2008). *J. Appl. Cryst.* **41**, 1057–1066.
Cherezov, V., Hanson, M. A., Griffith, M. T., Hilgart, M. C., Sanishvili, R., Nagarajan, V., Stepanov, S., Fischetti, R. F., Kuhn, P. & Stevens, R. C. (2009). *J. R. Soc. Interface*, **6**, S587–S597.
Cipriani, F. *et al.* (2006). *Acta Cryst.* D**62**, 1251–1259.
Cramer, P., Bushnell, D. A., Fu, J., Gnatt, A. L., Maier-Davis, B., Thompson, N. E., Burgess, R. R., Edwards, A. M., David, P. R. & Kornberg, R. D. (2000). *Science*, **288**, 640–649.
Cusack, S., Belrhali, H., Bram, A., Burghammer, M., Perrakis, A. & Riekel, C. (1998). *Nature Struct. Biol.* **5**, 634–637.
Flot, D., Mairs, T., Giraud, T., Guijarro, M., Lesourd, M., Rey, V., van Brussel, D., Morawe, C., Borel, C., Hignette, O., Chavanne, J., Nurizzo, D., McSweeney, S. & Mitchell, E. (2010). *J. Synchrotron Rad.* **17**, 107–118.
Gabadinho, J. *et al.* (2010). *J. Synchrotron Rad.* **17**, doi:10.1107/S0909049510020005.
Gether, U., Ballesteros, J. A., Seifert, R., Sanders-Bush, E., Weinstein, H. & Kobilka, B. K. (1997). *J. Biol. Chem.* **272**, 2587–2590.
Higuchi, Y., Okamoto, T. & Yasuoka, N. (1996). *J. Cryst. Growth*, **168**, 99–105.
Incardona, M.-F., Bourenkov, G. P., Levik, K., Pieritz, R. A., Popov, A. N. & Svensson, O. (2009). *J. Synchrotron Rad.* **16**, 872–879.
Ishmukhametov, R. R., Galkin, M. A. & Vik, S. B. (2005). *Biochim. Biophys. Acta*, **1706**, 110–116.
Jacquamet, L., Joly, J., Bertoni, A., Charrault, P., Pirocchi, M., Vernede, X., Bouis, F., Borel, F., Périn, J.-P., Denis, T., Rechatin, J.-L. & Ferrer, J.-L. (2009). *J. Synchrotron Rad.* **16**, 14–21.
Jacquamet, L., Ohana, J., Joly, J., Borel, F., Pirocchi, M., Charrault, P., Bertoni, A., Israel-Gouy, P., Carpentier, P., Kozielski, F., Blot, D. & Ferrer, J.-L. (2004). *Structure*, **12**, 1219–1225.
Lavault, B., Ravelli, R. B. G. & Cipriani, F. (2006). *Acta Cryst.* D**62**, 1348–1357.
Leal, R. M. F., Teixeira, S. C. M., Rey, V., Forsyth, V. T. & Mitchell, E. P. (2008). *J. Appl. Cryst.* **41**, 729–737.
Leslie, A. G. W., Powell, H. R., Winter, G., Svensson, O., Spruce, D., McSweeney, S., Love, D., Kinder, S., Duke, E. & Nave, C. (2002). *Acta Cryst.* D**58**, 1924–1928.
Lutter, R., Abrahams, J. P., van Raaij, M. J., Todd, R. J., Lundqvist, T., Buchanan, S. K., Leslie, A. G. W. & Walker, J. E. (1993). *J. Mol. Biol.* **229**, 787–790.
McPhillips, T. M., McPhillips, S. E., Chiu, H.-J., Cohen, A. E., Deacon, A. M., Ellis, P. J., Garman, E., Gonzalez, A., Sauter, N. K., Phizackerley, R. P., Soltis, S. M. & Kuhn, P. (2002). *J. Synchrotron Rad.* **9**, 401–406.
Moukhametzianov, R., Burghammer, M., Edwards, P. C., Petitdemange, S., Popov, D., Fransen, M., McMullan, G., Schertler, G. F. X. & Riekel, C. (2008). *Acta Cryst.* D**64**, 158–166.
Mueller-Dieckmann, C., Panjikar, S., Tucker, P. A. & Weiss, M. S. (2005). *Acta Cryst.* D**61**, 1263–1272.
Nurizzo, D., Mairs, T., Guijarro, M., Rey, V., Meyer, J., Fajardo, P., Chavanne, J., Biasci, J.-C., McSweeney, S. & Mitchell, E. (2006). *J. Synchrotron Rad.* **13**, 227–238.
Ohana, J., Jacquamet, L., Joly, J., Bertoni, A., Taunier, P., Michel, L., Charrault, P., Pirocchi, M., Carpentier, P., Borel, F., Kahn, R. & Ferrer, J.-L. (2004). *J. Appl. Cryst.* **37**, 72–77.
Okazaki, N., Hasegawa, K., Ueno, G., Murakami, H., Kumasaka, T. & Yamamoto, M. (2008). *J. Synchrotron Rad.* **15**, 288–291.
Paithankar, K. S., Owen, R. L. & Garman, E. F. (2009). *J. Synchrotron Rad.* **16**, 152–162.
Popov, A. N. & Bourenkov, G. P. (2003). *Acta Cryst.* D**59**, 1145–1153.
Pothineni, S. B., Strutz, T. & Lamzin, V. S. (2006). *Acta Cryst.* D**62**, 1358–1368.
Riekel, C., Burghammer, M. & Schertler, G. (2005). *Curr. Opin. Struct. Biol.* **15**, 556–562.
Sanchez-Weatherby, J., Bowler, M. W., Huet, J., Gobbo, A., Felisaz, F., Lavault, B., Moya, R., Kadlec, J., Ravelli, R. B. G. & Cipriani, F. (2009). *Acta Cryst.* D**65**, 1237–1246.
Sanishvili, R., Nagarajan, V., Yoder, D., Becker, M., Xu, S., Corcoran, S., Akey, D. L., Smith, J. L. & Fischetti, R. F. (2008). *Acta Cryst.* D**64**, 425–435.
Selmer, M., Dunham, C. M., Murphy, F. V. IV, Weixlbaumer, A., Petry, S., Kelley, A. C., Weir, J. R. & Ramakrishnan, V. (2006). *Science*, **313**, 1935–1942.
Sibanda, B. L., Chirgadze, D. Y. & Blundell, T. L. (2010). *Nature (London)*, **463**, 118–121.
Snell, G., Cork, C., Nordmeyer, R., Cornell, E., Meigs, G., Yegian, D., Jaklevic, J., Jin, J., Stevens, R. C. & Earnest, T. (2004). *Structure*, **12**, 537–545.
Soltis, S. M. *et al.* (2008). *Acta Cryst.* D**64**, 1210–1221.
Song, J., Mathew, D., Jacob, S. A., Corbett, L., Moorhead, P. & Soltis, S. M. (2007). *J. Synchrotron Rad.* **14**, 191–195.
Warne, T., Serrano-Vega, M. J., Baker, J. G., Moukhametzianov, R., Edwards, P. C., Henderson, R., Leslie, A. G. W., Tate, C. G. & Schertler, G. F. (2008). *Nature (London)*, **454**, 486–491.
Wimberly, B. T., Brodersen, D. E., Clemons, W. M. Jr, Morgan-Warren, R. J., Carter, A. P., Vonrhein, C., Hartsch, T. & Ramakrishnan, V. (2000). *Nature (London)*, **407**, 327–339.
Zhang, Z., Sauter, N. K., van den Bedem, H., Snell, G. & Deacon, A. M. (2006). *J. Appl. Cryst.* **39**, 112–119.